Scripta Materialia 148 (2018) 24–28

Contents lists available at ScienceDirect

Scripta Materialia

journal homepage: www.elsevier.com/locate/scriptamat

Regular Article

The effect of oxidation on the subsurface microstructure of a Ti-6Al-4V alloy

P.A.J. Bagot [a,*], A. Radecka [b,c], A.P. Magyar [d], Y. Gong [a], D.C. Bell [d], G.D.W. Smith [a], M.P. Moody [a], D. Dye [b], D. Rugg [c]

[a] Department of Materials, University of Oxford, Parks Road, Oxford, UK
[b] Department of Materials, Royal School of Mines, Imperial College, Prince Consort Road, South Kensington, London, UK
[c] Rolls-Royce plc, Elton Road, UK
[d] School of Engineering and Applied Sciences, Harvard University, Cambridge, MA, USA

ARTICLE INFO

Article history:
Received 24 October 2017
Received in revised form 4 January 2018
Accepted 11 January 2018
Available online xxxx

Keywords:
Titanium alloys
Oxidation
Atom probe tomography
α-case

ABSTRACT

Atom Probe Tomography (APT) and Transmission Electron Microscopy (TEM) are combined for examining α-case formation in Ti-6Al-4V, generated by air exposure at 800 °C. Below the oxide surface, the microstructure separates into a nanoscale mixture of the α-Ti and α_2 Ti_3Al phases, of compositions Ti70-O30 and Ti65-O10-Al20-V5 respectively. The α_2 phase exists either as bands or as nanoscale spherical precipitates. Nitrogen also penetrates the surface, but to a lesser extent, while vanadium partitions to α_2 or in distinctly separate phases. The results demonstrate that oxygen stimulates precipitation of α_2, helping to explain embrittlement produced in the O-enriched layer beneath the oxide.

Titanium alloys are a major aircraft engineering material, used in airframes/turbine engines owing to their excellent corrosion resistance and high specific fatigue strength. These advantages have also led to their use in chemical and biomedical applications. Alloy Ti-6Al-4V (in wt%, or Ti-10.2Al-3.6 in at.%) is regarded as the current workhorse of the aerospace industry, accounting for over half of global titanium alloy production [1,2].

For gas turbine engines, the maximum alloy operating temperature is limited by its tolerance to oxygen attack without excessive mechanical property degradation. For alpha-beta alloys, containing a hexagonal close-packed (hcp) α-phase and a body centred-cubic (bcc) β-phase, the practical upper limit is 315–400 °C [1]. Above ~480 °C a (TiO_2) scale forms on the alloy surface with an oxygen-rich solid solution beneath [3]. The latter is termed the 'α-case'. While oxygen stabilises and strengthens the α-Ti phase, typically yielding up to two-fold hardness increases [3], this layer is brittle and causes a marked deterioration in toughness and fatigue response, increasing component susceptibility to cracking [4,5].

Along with forming during operation, α-case can develop during processing, such as forging. There are concerns that shot peening, applied to place the surface into compression and enhance tolerance to surface scratches, can increase the uptake of oxygen by enhancing diffusion rates along defects [6]. The total α-case thickness depends on a range of processing variables [4], exposure conditions [3,7,8] cooling rate [4] and alloy composition [9]. After processing, α-case layers must be mechanically and/or chemically removed in costly and labour-intensive post-processing steps.

While in aerospace α-case layers are regarded as problematic, in biomedical applications their formation can be beneficial. Oxide layers on titanium implants increase hardness and reduce wear, while the α-case layer maintains attachment of the oxide to the metal, preventing ion dissolution into the body. A further benefit is that oxidised titanium has a Young's modulus comparable with bone [10]. Understanding the structure and optimum thickness of both oxide and α-case layers is key to improve implant performance.

Despite such motivation, there is a surprising lack of knowledge on α-case microstructures. They are commonly referred to simply as 'oxygen-rich layers', e.g. [3] yet hardness values vary considerably within the overall depth of 100s of μm. It is also not clear exactly where the oxygen atoms reside, nor how they affect the distribution of other species.

In this study, we use a combined experimental approach of Atom Probe Tomography (APT) and Transmission Electron Microscopy (TEM) to examine α-case formation in Ti-6Al-4V. APT provides a unique ability to examine the 3D atomic-scale structure of materials. Selected examples of Ti-alloy APT work include examining element partitioning [11], phase formation [12–16] and trace oxygen effects on mechanical properties [17,18].

Ti-6Al-4V samples were supplied by Rolls-Royce plc. The material was rolled in the α/β phase field and machined before vacuum annealing at 700 °C for 2 h. Thin sections (25 mm^2) were subsequently air exposed at 800 °C for 24 h to produce an oxide scale, before removal for air

* Corresponding author.
E-mail address: paul.bagot@materials.ox.ac.uk (P.A.J. Bagot).

https://doi.org/10.1016/j.scriptamat.2018.01.015
1359-6462/

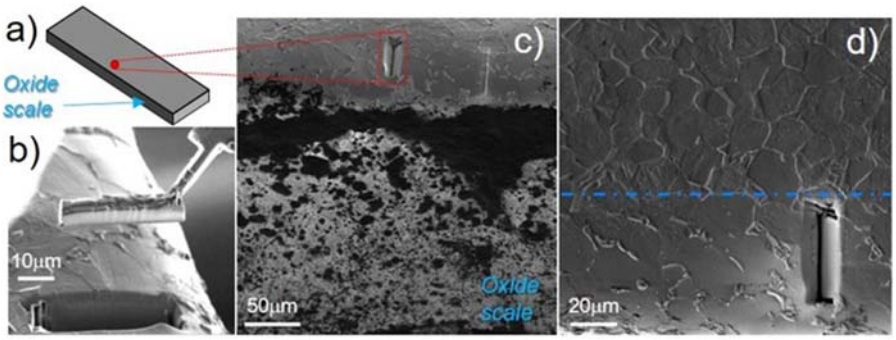

Fig. 1. a) Schematic showing APT sample extraction from cross-section of Ti-6Al-4V following exposure to air at 800 °C/24 h to generate an α-case. b) SEM image of extracted FIB lift-out sample prior to sharpening. c) SEM image showing sample extraction in relation to exposed surface. d) SEM image showing sample extraction and extent of microstructural changes. (For interpretation of the references to color in this figure, the reader is referred to the web version of this article.)

cooling. The high temperature chosen was intended to determine the upper extent of oxidation-induced changes.

Following oxidation, APT specimens were extracted from a cross-section near the exposed surface using a focussed ion beam (FIB) lift-out method. The lift-outs were fabricated using Zeiss NVision FIB or FEI Helios NanoLab 600 DualBeam instruments.

Samples were analysed using a LEAP™ 3000X HR equipped with a 532 nm laser (University of Oxford), and a 4000X HR with a 355 nm laser (School of Engineering and Applied Sciences, Harvard University). For this batch of material, the bulk alloy composition was confirmed in a prior APT study, which also confirmed the technique suitability for verifying known trace oxygen additions [18].

The locations of atom probe samples taken from the cross-sectioned alloy are summarised in Fig. 1. Prior X-ray diffraction studies have shown that at 800 °C outermost oxides are solely rutile (TiO_2), and that they spall above 800 °C/16 h [19], which is also noted in Fig. 1c. It is possible to quantify the penetration depth of the α case layer, which is approximately 60 μm (distance to dotted blue line in Fig. 1d).

The SEM images indicate an apparently uniform α-case layer, but it is immediately clear from Fig. 2a that this assumption does not hold at the nanoscale. The APT analysis (all in at.%) yields an overall composition of Ti67.6-O19.0-Al11.0-V2.4. However, the atom map and TEM images show the alloy has partitioned into two distinct phases with significantly different chemistries. A proximity histogram showing the chemical composition either side of a phase interface is illustrated in Fig. 2b. One phase has a composition of Ti69.7-O28.0-Al1.5-V0.9, consistent with the oxygen-rich α-Ti phase in the Ti-O phase diagram at 800 °C. The second contains more Al (and V) at the expense of O, with a composition of Ti63.8-O10.4-Al20.7-V5.1, matching an α_2 (Ti_3Al) intermetallic phase containing oxygen. The structure of this phase is backed by TEM diffraction data (shown in Supplementary Material, Fig. S1). It has been previously reported [16,20] that even very small Ti_3Al precipitates can be identified by TEM, as they produce superlattice reflections in selected area transmission electron diffraction (SAD) patterns [21]. Ti_3Al reflections occur symmetrically between the reflections from the alloy matrix along certain directions, and the lattice parameter of Ti_3Al is approximately twice that of matrix alpha [16]. Therefore, the extra diffraction spots seen at Fig. S1 originate from the Ti_3Al phase. The corresponding dark field image taken using the superlattice spot is shown in Fig. 3c, confirming the presence of both phases in this banded structure, with the α-phase dominant by volume (approximately 3–4:1).

For APT oxide analysis, the yield, mass resolution and stoichiometric accuracy can be improved using a UV laser-equipped instrument for various materials [22–24] including TiO_2 [25]. The field evaporation behaviour of oxides is also an active topic of investigation [26]. Therefore, to verify the nature of phases present, the same samples were also

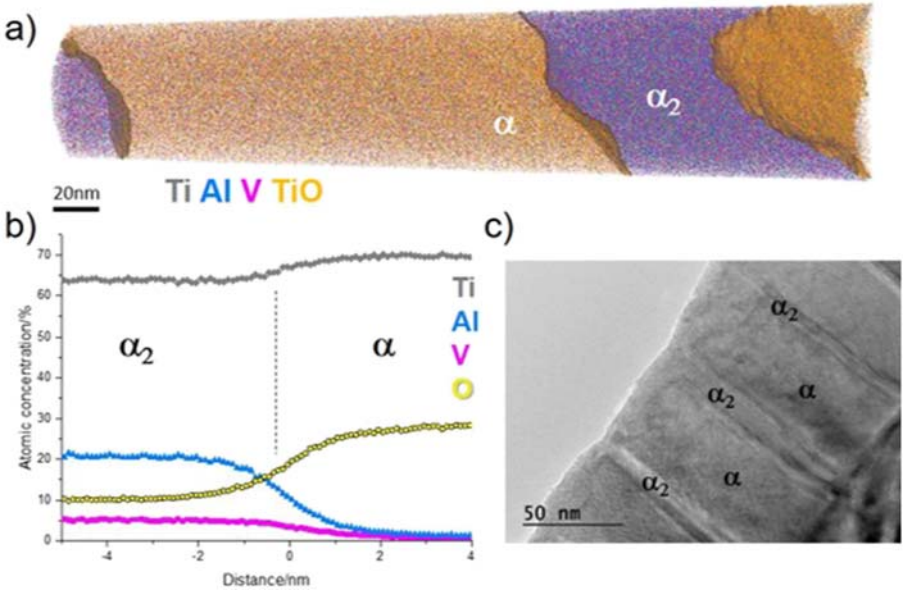

Fig. 2. a) Atom map of Ti-6-4 following exposure in air at 800 °C/24 h obtained on a LEAP 3000X HR, using TiO iso-concentration surfaces (37 at.%) to demarcate the two phase ($\alpha + \alpha_2$) banded microstructure. b) Proximity histogram demonstrating differences in phase compositions. c) Bright field TEM image from the same sample, confirming the presence of banded structures.

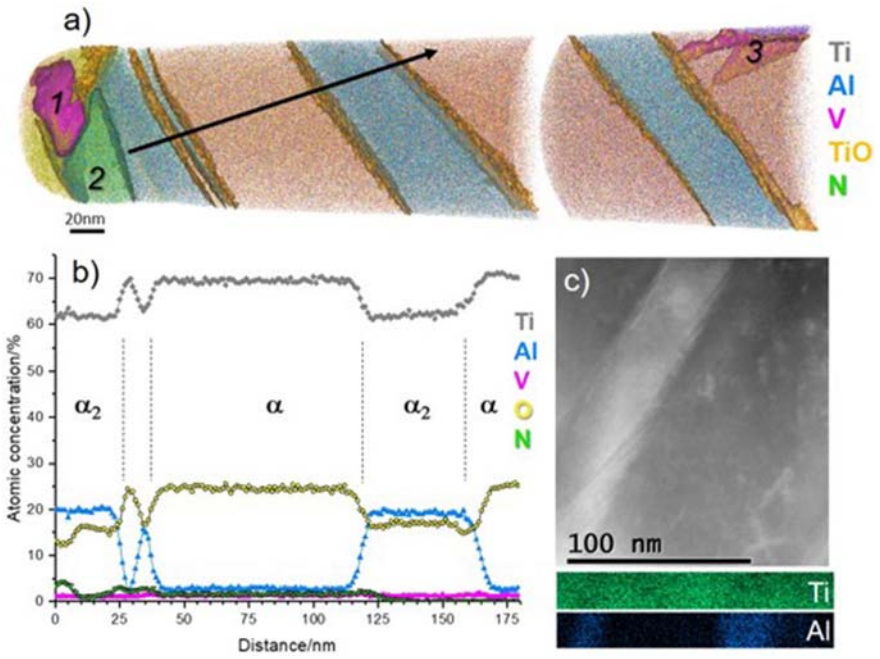

Fig. 3. a) Atom maps of Ti-6-4 following exposure in air at 800 °C/24 h obtained on a LEAP 4000X HR, using TiO iso-concentration surfaces (40%) to demarcate two phase (α + α2) banded microstructure. Also apparent are two V-rich regions (labelled '1', '3') and an Al-rich outer surface layer ('2'). b) 1D concentration profile generated along the direction of the black arrow in a). c) Dark field TEM image close-up image of banded structure confirming sharp interfaces. d) STEM-EDX map from the same sample showing Al-enrichment in two bands, presumed to be α_2.

examined on a LEAP 4000X HR system, Fig. 3. Comparing the atom maps in Figs. 3a and 2a, similar banded microstructures are seen, with the alternating phases identified in the 1D concentration profile of Fig. 3b. The α phase has a composition of Ti71.5-O24.1-Al2.9-V1.5, while the α_2 phase yields Ti61.1-O17.1-Al19.9-V1.5. Thus the phase chemistries are comparable on both instruments, and are in good agreement the predicted Ti-Al-O ternary phase diagram at 800 °C [27].

Less V is seen in both major phases, although additional chemically-distinct regions are also present, labelled '1', '2' and '3' in Fig. 3a. The regions at the surface are difficult to definitively identify as they contain significant amounts of O, C and in particular N. Nevertheless, they emphasize the inhomogeneity of the oxide-metal interface, in a similar manner to that seen in an oxidised superalloy [28]. Region '1' is a V-rich volume located near the interface, with a metal composition of Ti53.7-Al1.3-V4.0, also containing 35% N, 3.4% O and 0.8% C. Region '2' is Al-rich, with an alloy composition of Ti53.0-Al25.4-V0.6, including 19% N and 1.2% O. There is little in the phase literature to help identify such phases, although nitrogen stabilises the Ti α-phase in a similar manner to oxygen [29], while the Al-rich phase has a Ti:Al ratio consistent with Ti_2AlN nitride, known to be stable >1400 °C [30]. Interestingly, all nitrogen-containing species are confined to the near-surface region, in contrast to the extensive penetration of oxygen.

Deeper into the surface, the second V-rich region '3' has a composition of Ti62.5-Al17.8-V7.0-O12.4. The oxygen content is thus lower than either of the α and α_2 phases, which is likely a consequence of the higher level of V; the solubility limit of oxygen in vanadium is only around 7–8 at.% at 800 °C [31]. An effect of air exposure thus seems to be the partitioning of V into localised regions, resulting in large volumes of the near-surface microstructure depleted in V. Indeed, in a separate study, Energy-Dispersive X-ray analysis of an outer oxide formed at 650 °C also showed low V levels [19].

In addition to forming 'banded' microstructures, some samples extracted from the same region were found to form a different structure; a dense distribution of near-spherical nanoscale precipitates. A typical example is shown in Fig. 4, with the intermetallic atomic structure visible within two precipitates isolated by the iso-concentration surfaces in Fig. 4b. The global composition of the entire volume is Ti69.2-O19.3-Al9.2-V2.0, very similar to the global composition of the 'banded' sample in Fig. 2. The individual compositions of the two phases are Ti70.8-O21.1-Al6.2-V1.6 (matrix) and Ti66.0-O10.0-Al20.8-V2.8 (clusters), again identifying them as α and α_2 respectively. The TEM image of Fig. 4d confirms the size, shape and high number density of these α_2 precipitates, illustrating that the two phases can co-exist as different morphologies within the same volume - both banded and precipitate forms were observed from the same sample lift-out (~25 × 5 × 3 μm).

The overarching result from all APT datasets and TEM images is that following exposure the alloy segregates into two main phases, which both contain different levels of oxygen. The available literature on oxygen solubilities suggests a maximum level of around 34 at.% in α-Ti [32], whereas in Ti_3Al a theoretical maximum of ~10–14 at.% has been reported [33,34]. These closely match the levels seen in the APT data for α and α_2 phases, confirming oxygen saturation, and there is negligible differential loss in oxygen when analysed by either type of atom probe. This contrasts with prior studies using various electron beam methods to examine oxygen levels in various Ti-alloys, which all admit to issues with accurate quantification [33,35–37]. Supporting calculations were also carried out using Thermo-Calc 2017a with the ThermoTech Ti-based Alloys Database (v3) at 800 °C, using the bulk compositions derived by APT. These suggest oxygen contents ~19 at.% are sufficient to completely suppress the β phase, producing a near 50:50 mix of α and α_2, in good agreement with the experiments.

β-phase in the pre-exposed alloy may also be contributing to the observed microstructures. O diffusion is around two orders of magnitude faster in β than in α [38]. This suggests that, in a transformed β grain consisting of alternating α and β plates, O could diffuse down the β film, leading to growth of the secondary α plate until the β is completely consumed. α_2 could then precipitate in the lower-O core of the original secondary α plate. Therefore, the banded structures identified in Figs. 2 and 3 might be a consequence of the oxidation of the α/β colony. In contrast, where the O content gradually increases in a much larger primary α grain, precipitation of near-spherical α_2 nanoscale precipitates such as shown in Fig. 4 occurs, because there are no prior α/β interfaces present.

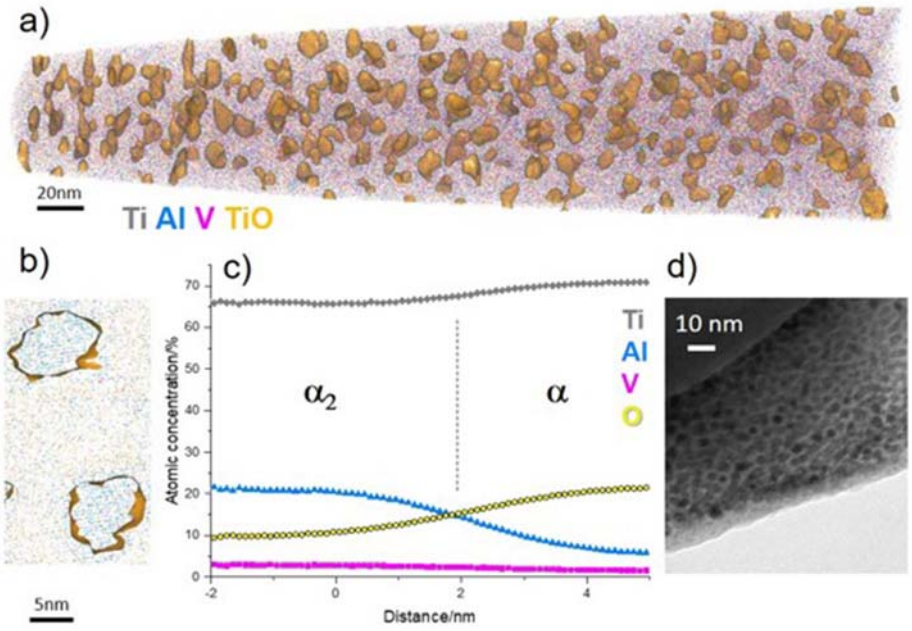

Fig. 4. a) Atom map of Ti-6Al-4V following exposure in air at 800 °C/24 h obtained on a LEAP 4000X HR, using 25% TiO iso-concentration surfaces to demarcate α_2 clusters. b) 1.5 nm thick slice through atom map, illustrating parallel atomic lattice planes in clusters. c) Proxigram analysis through the phases in a). d) Bright field TEM image of the clusters.

The overall oxidation kinetics can be conventionally examined by weight gain ΔW per surface area A, with rate constant K and reaction index n:

$$\Delta W/A = Kt^{1/n}$$

For Ti-6Al-4V oxidation kinetics have been shown to follow a parabolic relationship ($n = 2$) up to 800 °C for 200 h in dry air [3,8,37]. From this, it has been quite reasonably assumed that diffusion of oxygen to form an α-case would also follow a straightforward parabolic dependence [37]; the combined APT/TEM data presented here clearly shows more complex microstructures however. The total α-case depth (or 'oxygen diffusion zone' (ODZ)) can be predicted using the empirical relationship derived by Guleryuz [8]:

$$X_{ODZ} = 10^6 \times \theta^{0.5}$$

where θ is a temperature-compensated time parameter, following Arrhenius-type behaviour of the form $\theta = t \times \exp(-Q/RT)$. Using the known exposure parameters here along with a quoted activation energy Q of 202 kJ mol^{-1} [8] yields an X_{ODZ} of 59 μm, in very close agreement with 60 μm measured in Fig. 1d.

While mechanical property measurements were not a focus in the current work, microhardness measurements can be correlated to oxygen content [4]. Using the linear model presented in [4] with our oxygen level returns an expected hardness of ~760 HV, in good agreement with hardness tests at similar conditions [19]. Other mechanical properties such as ultimate and 0.2% proof tensile strengths appear unaltered by similar depths of α-case layers [9], while tensile elongation strength, bending fatigue strength and ductility all deteriorate in various Ti-alloys with increasing heating times/oxygen levels and α-case depths [39]. Removal of these layers using a pickling treatment recovers the original mechanical properties, confirming the role of oxygen-rich layers in altering properties [9].

As a final point, it is very interesting to observe that O additions to Ti result in precipitation of the α_2 phase, which is strongly implicated in the loss of fatigue endurance in titanium alloys [40]. For lower exposure temperatures, where most aluminium-alloyed α-Ti is in any case metastable with respect to α_2 precipitation, this may explain why beyond a certain point, any solution strengthening benefit from oxygen begins to be outweighed by a loss in fatigue behaviour and ductility.

The insight into microstructural complexities in terms of both chemistry and morphology highlights the need for further dedicated high-resolution characterisation studies, examining formation kinetics, influence of exposure conditions, cooling rates and alloy composition on the exact microstructures formed. These are important not only to understand fundamental mechanisms of oxygen-driven behaviours, but also for engineering relevance within in-service components.

Supplementary data to this article can be found online at https://doi.org/10.1016/j.scriptamat.2018.01.015.

Acknowledgments

PAJB acknowledges the Royal Academy of Engineering for an Industrial Secondment award to Rolls-Royce plc, and travel support from The Queen's College, Oxford. DD was funded by EPSRC (EP/K034332/1). Prof. Roger Reed (Department of Engineering Science, University of Oxford) is thanked for access to Thermo-calc software.

References

[1] R. Boyer, Mater. Sci. Eng. A 213 (1996) 103.
[2] M. Peters, J. Kumpfert, C.H. Ward, C. Leyens, Adv. Eng. Mater. 5 (2003) 419.
[3] R. Gaddam, B. Sefer, R. Pederson, M.L. Antti, IOP Conf. Ser. Mater. Sci. Eng. 48 (2013), 012002.
[4] K.S. Chan, M. Koike, B.W. Johnson, T. Okabe, Metall. Mater. Trans. A 39 (2008) 171.
[5] T. Parthasarathy, W. Porter, S. Boone, R. John, P. Martin, Scr. Mater. 65 (2011) 420.
[6] M. Thomas, T. Lindley, D. Rugg, M. Jackson, Acta Mater. 60 (2012) 5040.
[7] I. Gurappa, J. Mater. Sci. Lett. 22 (2003) 771.
[8] H. Guleryuz, H. Cimenoglu, J. Alloys Compd. 472 (2009) 241.
[9] H. Fukai, H. Iizumi, K.-N. Minakawa, C. Ouchi, ISIJ Int. 45 (2005) 133.
[10] C. Munuera, T.R. Matzelle, N. Kruse, M.F. López, A. Gutiérrez, J.A. Jiménez, C. Ocal, Acta Biomater. 3 (2007) 113.
[11] D. Larson, C. Liu, M. Miller, Mater. Sci. Eng. A 270 (1999) 1.
[12] H. Liew, G.D.W. Smith, A. Cerezo, D.J. Larson, Mater. Sci. Eng. A 270 (1999) 9.
[13] S. Nag, R. Banerjee, H.L. Fraser, J. Mater. Sci. 44 (2008) 808.
[14] J. Coakley, V.A. Vorontsov, N.G. Jones, A. Radecka, P.A.J. Bagot, K.C. Littrell, R.K. Heenan, F. Hu, A.P. Magyar, D.C. Bell, D. Dye, J. Alloys Compd. 646 (2015) 946.
[15] T. Li, D. Kent, G. Sha, J.M. Cairney, M.S. Dargusch, Scr. Mater. 117 (2016) 92.
[16] A. Radecka, J. Coakley, V.A. Vorontsov, T.L. Martin, P.A.J. Bagot, M.P. Moody, D. Rugg, D. Dye, Scr. Mater. 117 (2016) 81.
[17] S.L. Draper, D. Isheim, Intermetallics 22 (2012) 77.

[18] D. Rugg, T.B. Britton, J. Gong, A.J. Wilkinson, P.A.J. Bagot, Mater. Sci. Eng. A 599 (2014) 166.
[19] S. Kumar, T.S.N. Sankara Narayanan, S. Ganesh Sundara, S.K. Seshadri Raman, Mater. Chem. Phys. 119 (2010) 337.
[20] Z. Wu, C.L. Qiu, V. Venkatesh, H.L. Fraser, R. Williams, G.B. Viswanathan, M. Thomas, S. Nag, R. Banerjee, M. Loretto, Metall. Mater. Trans. A 44 (2013) 1706.
[21] A. Woodfield, P. Postans, M. Loretto, R. Smallman, Acta Metall. 3 (1998) 507.
[22] Y. Chen, T. Ohkubo, K. Hono, Ultramicroscopy 111 (2011) 562.
[23] A. La Fontaine, B. Gault, A. Breen, L. Stephenson, A.V. Ceguerra, L. Yang, T. Dinh Nguyen, J. Zhang, D.J. Young, J.M. Cairney, Ultramicroscopy 159 (2015) 354.
[24] B. Valderrama, H.B. Henderson, J. Gan, M.V. Manuel, J. Nucl. Mater. 459 (2015) 37.
[25] A. Vella, B. Mazumder, G. Da Costa, B. Deconihout, J. Appl. Phys. 110 (2011), 044321.
[26] M. Karahka, H.J. Kreuzer, Ultramicroscopy 132 (2013) 54.
[27] K.L. Luthra, Oxid. Met. 36 (1991) 475.
[28] S. Pedrazzini, D.J. Child, G. West, S.S. Doak, M.C. Hardy, M.P. Moody, P.A.J. Bagot, Scr. Mater. 113 (2016) 51.
[29] H. Ogden, R. Jafee, The Effects of Carbon, Oxygen, and Nitrogen on the Mechanical Properties of Titanium and Titanium Alloys-TML Report, Technical Report 20, Office of Assistant Secretary of Defense for Research and Development, 1955.
[30] I.M. Low, W.K. Pang, S.J. Kennedy, R.I. Smith, J. Eur. Ceram. Soc. 31 (2011) 159.
[31] S.A.O. Hare, R.A. McCune, M.P. Krug, J. Less-Common Met. 21 (1970) 115.
[32] J.L. Murray, H.A. Wreidt, J. Phase Equilib. 8 (1987) 148.
[33] K. Das, P. Choudhury, S. Das, J. Phase Equilib. 23 (2002) 525.
[34] C.Y. Jones, W.E. Luecke, E. Copland, Intermetallics 14 (2006) 54.
[35] F. Dettenwanger, M. Schu, Oxid. Met. 54 (2000) 121.
[36] A.R. Ebrahimi, F. Zarei, R.A. Khosroshahi, Surf. Coat. Technol. 203 (2008).
[37] R. Gaddam, B. Sefer, R. Pederson, M.-L. Antti, Mater. Charact. 99 (2015) 166.
[38] G. Lütjering, J.C. Williams, Titanium, Springer, Berlin Heidelberg, 2007.
[39] H. Maier, R. Teteruk, H. Christ, Metall. Mater. Trans. A 31 (2000) 431.
[40] M. Brandes, Creep, Fatigue and Deformation of Alpha and Alpha-Beta Titanium Alloys at Ambient Temperature(Ph.D. thesis) Ohio State University, 2008.